Dynamics of semiconductor lasers with two-dimensional distributed feedback

N. S. Ginzburg,[1,2] V. R. Baryshev,[1,*] A. S. Sergeev,[1] and A. M. Malkin[1,2]
[1]*Institute of Applied Physics, Russian Academy of Science, Nizhny Novgorod, Russia*
[2]*Nizhny Novgorod State University, Nizhny Novgorod, Russia*
(Received 6 February 2015; published 7 May 2015)

We develop a nonlinear model of a laser exploiting two-dimensional (2D) distributed feedback (2D DFL). This feedback mechanism can be realized in a 2D Bragg resonator formed by a dielectric structure with the thickness having double-periodical sinusoidal or chessboard modulation. A 2D Bragg resonator is shown to possess high selectivity over both the longitudinal and the transverse coordinates and to have fundamental modes in the center of the forbidden band gap. Within the semiclassical approach, we study the nonlinear dynamics of 2D DFL and demonstrate spatial synchronization of radiation from an extended active medium. Specific features of 2D DFL operation with active medium amplifying modes of TM and TE (quantum-well lasers) polarization are also discussed.

DOI: 10.1103/PhysRevA.91.053806 PACS number(s): 42.55.Px, 42.60.Da, 42.60.Lh, 42.70.Qs

I. INTRODUCTION

Two-dimensional (2D) distributed feedback can be considered an effective method for generation of spatially coherent radiation from a broad class of sources based both on principles of classical [1–3] and quantum electronics [4–10]. In the case of a spatially extended active medium, a 2D feedback mechanism gives rise to transverse energy fluxes which synchronize radiation from different parts of this medium. For realization of 2D feedback, one can use 2D Bragg resonators. In the microwave frequency band such resonator can be a planar metallic waveguide with shallow double-periodic corrugation of side walls. In optics, similar structures can correspond to a dielectric film with a thickness having double-periodic modulation (Fig. 1). Substantial progress has been achieved recently in the experimental realization of the planar and coaxial free electron masers (FEMs) exploiting 2D feedback driven by large-size sheet and tubular electron beams [11–14]. In these experiments, narrow-band generation at frequencies close to those of the fundamental modes of 2D Bragg resonators was observed for the oversize factor (ratio of beam width to the wavelength) of about 20–30.

In this paper, we study the possibility of implementing 2D feedback in semiconductor lasers. These lasers combine high energy efficiencies with compact dimensions and can reach up to the 1 W output power level in continuous-wave regimes. Typically, an active region of a semiconductor laser is an epitaxially grown multilayer planar-shaped structure which is sufficiently large in two dimensions to provide high gain, while the third dimension is generally used for electric contacts and heat dissipation. Those structures often include Bragg grating layers [15–17] used for improvement of frequency stability. However, traditional one-dimensional (single-periodic) gratings are unable to solve the laser beam quality problem completely because they are unable to synchronize radiation in the case of large transverse size of the active medium. As a result, radiation quality suffers from multimode operation. In many practical realizations, the direction patterns are wide and irregular, laser beams have shorter coherence distances, and focusing spots significantly exceed diffraction limits [18,19]. Various complex gratings for improving beam quality were proposed, including circular, curved, and angled Bragg structures [20–25].

As an alternative method, we consider in the present paper a possibility of spatial synchronization of laser radiation by implementing 2D distributed feedback. In semiconductor lasers, 2D feedback can be realized by 2D Bragg resonators, i.e., dielectric films with double-periodic modulation of thickness providing coupling between modes of planar dielectric waveguides. Most types of active media amplify waves regardless of their polarization. Nevertheless, in the case of commonly used heterostructures where the active layer is a 2D quantum well, gain of TM modes is typically weak [26,27]. In this case, predominant amplification of TE modes takes place. However, coupling of TE waves of a planar dielectric waveguide is not possible in a 2D Bragg resonator (see Sec. II). Thus, to arrange 2D distributed feedback in quantum-well lasers one should employ coupling of TE and TM modes. In this case, two partial wave beams of the TE type can be amplified by the active medium while two other partial wave beams of the TM type propagate in the transverse direction and synchronize radiation of the whole active medium via coupling with TE modes.

The paper is organized as follows. In Sec. II, based on the coupled-wave method, we describe selective properties of a 2D Bragg resonator formed by double-corrugated dielectric film. Our consideration includes coupling of both TM and TE modes. In Sec. III, in the frame of the semiclassical approach, we study nonlinear dynamics of a laser with 2D distributed feedback (2D DFL). Specific features of laser operation with all four partial waves amplified by active media and with only two of them experiencing amplification while two others are responsible for spatial synchronization (quantum-well lasers) are studied. The scalability features of the 2D DFL are discussed to demonstrate a possibility of increasing the output power with increasing dimensions of active medium while keeping the synchronization regime intact.

II. EIGENMODES OF A DIELECTRIC 2D BRAGG RESONATOR

A 2D Bragg resonator formed by a planar dielectric structure with a thickness having double-periodic modulation

*baryshev@appl.sci-nnov.ru

 ©2015 American Physical Society

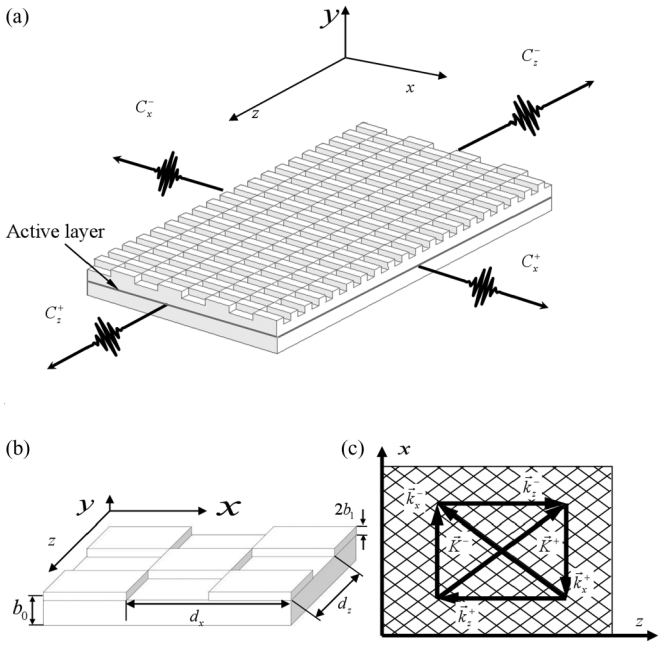

FIG. 1. (a) Scheme of a 2D DFL. (b) A close-up of the chessboard grating. (c) Diagram illustrating the coupling of the partial modes on the 2D Bragg grating. Here $\vec{k}_x^{\pm} = \pm h\vec{x}_0$, $\vec{k}_z^{\pm} = \pm h\vec{z}_0$, $\vec{K}^{\pm} = \bar{h}\vec{x}_0 \pm \bar{h}\vec{z}_0$; $\vec{x}_0$ and $\vec{z}_0$ are the unit vectors directed in the x and z directions, correspondingly.

is shown in Figs. 1(a) and 1(b). In the idealized case the modulation can be sinusoidal:

$$b(x,z) = b_0 + b_1[\cos(\bar{h}_x x + \bar{h}_z z) + \cos(\bar{h}_x x - \bar{h}_z z)], \quad (1)$$

where b_0 is the mean thickness of a dielectric layer, b_1 is the modulation amplitude, $\bar{h}_{x,z} = 2\pi/d_{x,z}$, and d_x and d_z are the periods over the x and z coordinates, correspondingly. For simplicity, we consider the structure characterized by a dielectric permittivity ε located in an optically transparent background medium with dielectric permittivity equal to 1, though the consideration can be readily generalized on more complicated situations. This structure provides coupling and mutual scattering of the four partial wave beams [see Fig. 1(c)] given by vector potential

$$\vec{A} = \mathrm{Re}\big[\big(\vec{a}_1(y)C_z^+ e^{-ih_z z} + \vec{a}_1^*(y)C_z^- e^{ih_z z} + \vec{a}_2(y)N_0 C_x^+ e^{-ih_x x} + \vec{a}_2^*(y)N_0 C_x^- e^{ih_x x}\big)e^{i\omega t}\big], \quad (2)$$

where $\vec{a}_{1,2}(y)$ denote the transverse profiles of the modes of planar dielectric waveguide propagating correspondingly in $\pm z$ and $\pm x$ directions; $C_{x,z}^{\pm}(x,z,t)$ are the slowly varying complex amplitudes of the partial waves. We put $|\vec{a}_{1,2}(y=0)| = 1$; $N_0 = (\int_{-\infty}^{\infty} \varepsilon(y)|\vec{a}_2(y)|^2 dy / \int_{-\infty}^{\infty} \varepsilon(y)|\vec{a}_1(y)|^2 dy)^{1/2}$ is a normalizing coefficient. Effective coupling takes place when Bragg resonance conditions,

$$h_x \approx \bar{h}_x, \quad h_z \approx \bar{h}_z, \quad (3)$$

are satisfied. In terms of the photonic band-gap structures' symmetry points, we operate in the vicinity of the M point [28] in the reciprocal space of two-dimensional lattice, where four partial wave beams are coupled.

Note that for practical applications, similarly to the case of 2D Bragg resonators formed by planar metallic waveguide with shallow corrugation of side walls [11–14], it is sufficient to substitute the sine modulation (1) by a chessboard function [see Fig 1(a)]:

$$b(x,z) = b_0 + b_1 f(x) f(z),$$
$$f(\xi) = \begin{cases} 1, & 2q\pi/\bar{h}_\xi < \xi < (2q+1)\pi/\bar{h}_\xi \\ -1, & (2q-1)\pi/\bar{h}_\xi < \xi < 2q\pi/\bar{h}_\xi, \quad q = 1,2\ldots \end{cases}. \quad (4)$$

For small modulation depth b_1, we use an approach described in Ref. [29]. We introduce modes of the regular dielectric waveguide (at $b_1 = 0$) and then derive coupling equations where the coupling coefficients α_{12} between two modes arising due to nonzero perturbation $\Delta\varepsilon(x,y,z)$ are proportional to

$$\alpha_{12} \sim \int \Delta\varepsilon \vec{E}_1 \vec{E}_2 dx dy dz, \quad (5)$$

where $\vec{E}_1$ and $\vec{E}_2$ are electric fields of those modes.

Eigenwaves of regular planar dielectric waveguides possess either TE or TM polarization. In the case of a one-dimensional (1D) Bragg structure, the coupling between waves of both polarizations takes place. That is not the case for 2D Bragg structures studied here, where the Bragg condition is satisfied for the mutual scattering between partial waves C_x and C_z propagating in mutually orthogonal directions.

We assume that the thickness of the dielectric layer b_0 is limited by the condition of $kb_0\sqrt{(\varepsilon-1)} < \pi$ under which, in the frequency range specified by the active medium amplification band, there is only one propagating TM wave and one propagating TE wave.

Nonzero vector potential components of TM-polarized partial waves can be presented in the form [29]

$$a_{1y}^{\mathrm{TM}}(y) = a_{2y}^{\mathrm{TM}}(y) = \cos g_{\mathrm{TM}} y,$$
$$a_{1z}^{\mathrm{TM}}(y) = a_{2x}^{\mathrm{TM}}(y) = \frac{-ig_{\mathrm{TM}}}{h} \sin g_{\mathrm{TM}} y, \quad (6)$$

at $|y| < l_y/2$,

$$a_{1y}^{\mathrm{TM}}(y) = a_{2y}^{\mathrm{TM}}(y) = \frac{g_{\mathrm{TM}}}{p_{\mathrm{TM}}} \sin\left(\frac{g_{\mathrm{TM}} b_0}{2}\right) e^{-p_{\mathrm{TE}}|y|},$$
$$a_{1z}^{\mathrm{TM}}(y) = a_{2z}^{\mathrm{TM}}(y) = \frac{-ig_{\mathrm{TM}}}{h} \sin\left(\frac{g_{\mathrm{TM}} b_0}{2}\right) e^{-p_{\mathrm{TE}}|y|}, \quad (7)$$

at $|y| > l_y/2$. Here $k = \omega/c$, $g_{\mathrm{TM}} = \sqrt{\varepsilon k^2 - h^2}$, and $p_{\mathrm{TM}} = \sqrt{h^2 - k^2}$ are the transverse wave numbers inside and outside the dielectric which for a given ε, k, and b_0 can be found from the characteristic equation for the symmetric TM waves of a dielectric waveguide:

$$p_{\mathrm{TM}} = \sqrt{(\varepsilon-1)k^2 - g_{\mathrm{TM}}^2} = \frac{g_{\mathrm{TM}}}{\varepsilon} \tan\left(\frac{g_{\mathrm{TM}} b_0}{2}\right). \quad (8)$$

TE-polarized fields are given by vector potential

$$a_{1x}^{\mathrm{TE}}(y) = a_{2z}^{\mathrm{TE}}(y) = i \cos g_{\mathrm{TE}} y, \quad (9)$$

at $|y| < l_y/2$,

$$a_{1x}^{\mathrm{TE}}(y) = a_{2z}^{\mathrm{TE}}(y) = \frac{-i g_{\mathrm{TE}}}{h} \sin\left(\frac{g_{\mathrm{TE}} b_0}{2}\right) e^{-p_{\mathrm{TE}}|y|}, \quad (10)$$

at $|y| > l_y/2$. Transverse wave numbers $g_{\mathrm{TE}} = \sqrt{\varepsilon k^2 - h^2}$ and $p_{\mathrm{TE}} = \sqrt{h^2 - k^2}$ can be found from the characteristic equation

$$\sqrt{(\varepsilon - 1)k^2 - g_{\mathrm{TE}}^2} = g_{\mathrm{TE}} \tan\left(\frac{g_{\mathrm{TE}} b_0}{2}\right). \quad (11)$$

Comparing (6) and (7), and (9) and (10), one can see that $\vec{a}_1^{\mathrm{TE}}\vec{a}_2^{\mathrm{TE}} = 0$, while $\vec{a}_1^{\mathrm{TM}}\vec{a}_2^{\mathrm{TM}} = \vec{a}_{1y}^{\mathrm{TM}}\vec{a}_{2y}^{\mathrm{TM}} \neq 0$ and $\vec{a}_1^{\mathrm{TE}}\vec{a}_2^{\mathrm{TM}} = \vec{a}_{1x}^{\mathrm{TE}}\vec{a}_{2x}^{\mathrm{TM}} \neq 0$. The same applies to the electric fields of those waves. According to (5), this means that coupling of TE-polarized waves does not take place. The most effective coupling exists between TM modes, while in the considered case of single-mode waveguide when $g_{\mathrm{TM}} \ll h$ the coupling coefficient of TE-TM modes is much smaller by a factor of $\frac{g_{\mathrm{TM}}}{h}$.

Equations for coupling between four TM waves as well as for coupling between two TE and two TM waves are presented below. We show that in both of these cases, interaction can be described by a set of equations taking similar form; the difference between the two cases amounts to a difference in the coefficients and normalizations.

A. Coupling of four TM-polarized waves

In this case, all partial waves at the same frequency have the same wave number over the y axis, $h_x = h_z = h$, leading to $\bar{h}_x = \bar{h}_z = \bar{h}$. Thus, in this case periods of dielectric layer modulation in the x and z directions must be the same to provide coupling between those modes. Mutual coupling and scattering of four partial wave beams $C_z^+\vec{a}_1^{\mathrm{TM}}, C_x^+\vec{a}_2^{\mathrm{TM}}$, $C_z^-\vec{a}_1^{\mathrm{TM}*}, C_x^-\vec{a}_2^{\mathrm{TM}*}$ given by (2), (6), and (7) on a 2D Bragg structure under the geometrical optics approximation can be described by the system of equations [10]:

$$\begin{aligned} \frac{\partial C_z^{\pm}}{\partial z} \mp i\delta C_z^{\pm} \pm i\alpha(C_x^+ + C_x^-) = 0, \\ \frac{\partial C_x^{\pm}}{\partial x} \mp i\delta C_x^{\pm} \pm i\alpha(C_z^+ + C_z^-) = 0. \end{aligned} \quad (12)$$

Here $\delta = h(\omega) - \bar{h}$ is the deviation from the frequency of the exact Bragg resonance and α is the coupling coefficient, which by implementing a method developed in [10], can be presented in the form

$$\alpha = \frac{\nu b_1 h}{4} \frac{(\varepsilon - h^2/k^2)(1 + 1/\varepsilon^2)}{(h^2/\varepsilon^2 k^2 + h^2/k^2 - 1)b_0 + 2(h^2 - k^2)^{-1/2}}, \quad (13)$$

where $\nu = 1$ for the case of a sinusoidal (1) and $\nu = 16/\pi^2$ for the case of a chessboard (4) modulation patterns.

Obviously, the coupled-wave theory presented in this paper is valid for weak coupling, $\alpha \ll h$. We should emphasize that by choosing corrugation patterns given by (1) or (4), we deliberately excluded direct coupling of counterpropagating partial waves $C_x^{\pm} \to C_x^{\mp}$, $C_z^{\pm} \to C_z^{\mp}$. Note also that Eq. (12) is written in the geometric optics approximation valid at large Fresnel parameters,

$$l_x^2/\lambda l_z \gg 1,\ l_z^2/\lambda l_x \gg 1, \quad (14)$$

when diffraction effects for every wave beam can be neglected.

B. Coupling of two TE- and two TM-polarized waves

Wave numbers of TE and TM waves are different for a given thickness b_0 of the dielectric waveguide at the same frequency. Accordingly, grid constants $\bar{h}_x$ and $\bar{h}_z$ have to be different to enable the mutual scattering of the waves [Fig. 1(c)]. However, the system of equations describing the coupling between the four waves $C_z^+\vec{a}_1^{\mathrm{TE}}, C_x^+\vec{a}_2^{\mathrm{TM}}, C_z^-\vec{a}_1^{\mathrm{TE}*}, C_x^-\vec{a}_2^{\mathrm{TM}*}$ given by (2), (6), and (7), and (9) and (10), can still be reduced to the form (12), where $\delta = (\omega - \bar{\omega})/v_g$ is the Bragg resonance detuning, coordinates $\tilde{x} = xr^{-1}, \tilde{z} = zr$, and amplitudes $\tilde{C}_x^{\pm} = C_x^{\pm} r^{-1/2}$, $\tilde{C}_z^{\pm} = C_z^{\pm} r^{1/2}$ should be used instead of x, z, and $C_{x,z}^{\pm}$. Here we introduce the notation

$$r = \sqrt{v_{gx}/v_{gz}},\ \ v_g = \sqrt{v_{gx} v_{gz}}, \quad (15)$$

where v_{gx} and v_{gz} are the group velocities of the lowest TM and TE waves of the regular dielectric waveguide. The coupling coefficient can be presented in the form [10]

$$\alpha = \frac{\nu b_1}{\sqrt{b^{\mathrm{TE}} b^{\mathrm{TM}}}} \frac{\sqrt{\varepsilon - 1}(\varepsilon^2 + 1)}{8\sqrt{\varepsilon}} \left(\frac{g_{\mathrm{TE}} p_{\mathrm{TE}}}{\sqrt{h_z^3}}\right) \times \left(\frac{p_{\mathrm{TM}}}{\sqrt{h_x\left(g_{\mathrm{TM}}^2 + \varepsilon^2 p_{\mathrm{TM}}^2\right)}}\right), \quad (16)$$

where

$$\begin{aligned} b^{\mathrm{TE}} &= b_0 + \frac{2}{\sqrt{h_z^2 - \bar{k}^2}}, \\ b^{\mathrm{TM}} &= b_0 + \frac{2}{\sqrt{h_x^2 - \bar{k}^2}\left(h_x^2/\varepsilon\bar{k}^2 + h_x^2/\bar{k}^2 - 1\right)}, \end{aligned} \quad (17)$$

are the effective waveguide thicknesses for TE and TM modes. It should be noted that for the same modulation amplitude the coupling coefficient given by (16) is much smaller than the one given by (13) for the case of TM modes coupling.

C. Normal waves of an unbounded 2D Bragg structure

Presenting a solution of Eq. (12) in the form $\sim e^{i(\Lambda_x x + \Lambda_z z)}$, one obtains the dispersion equation for the normal waves of an unbounded 2D Bragg structure near the Bragg resonance (3),

$$\left(\delta^2 - \Lambda_x^2\right)\left(\delta^2 - \Lambda_z^2\right) - 4\alpha^2\delta^2 = 0. \quad (18)$$

At $\delta > 0$, the dispersion characteristics $\delta(\Lambda_x, \Lambda_z)$ plotted in Fig. 2 are represented by two sheets (at $\delta < 0$, the solution is mirror symmetric to that shown in the figure). Sheet "1" intersects the vertical axis at the point $\delta/\alpha = 2$ (its mirror counterpart intersects this axis at $\delta/\alpha = -2$). These points correspond to the extrema of the function $\delta(\Lambda_x, \Lambda_z)$ at which the minima of the group velocities of normal waves are achieved. Two sets of the high-Q eigenmodes of the 2D Bragg resonator are located near these points as shown below. These modes are similar to those of a conventional 1D Bragg resonator. A specific feature of a 2D Bragg structure consists in

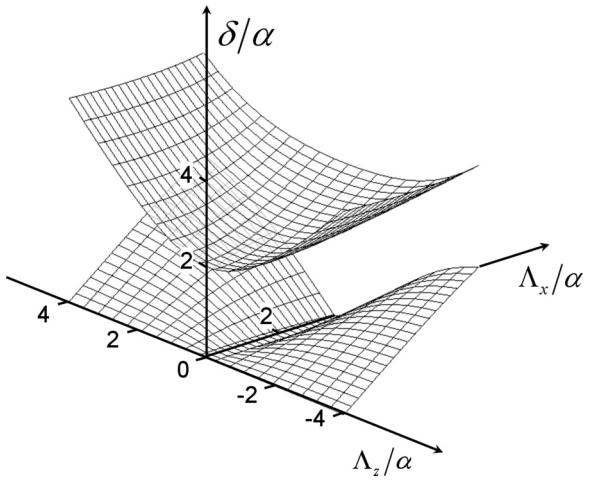

FIG. 2. Dispersion characteristics of the normal waves of 2D Bragg structures at $\delta > 0$.

the presence of the sheet "2" which intersects the vertical axis at the point $\delta = 0$. Not only the normal wave group velocity, but also its derivatives tend to zero in the vicinity of $\Lambda_x = \Lambda_z = 0$ for this sheet leading to formation of a third set of high-Q modes there.

D. Eigenmodes of a 2D Bragg resonator (analytical approach)

Next, we find the eigenmode spectrum of 2D Bragg structure in the proximity of the Bragg resonance (3) for a corrugation area on the dielectric film with finite sizes of l_x, l_z along corresponding axis. To find those eigenmodes, one should apply the boundary conditions at the edges of the modulation area. In assumption that the external energy fluxes are absent, these conditions acquire the form

$$C_z^+|_{z=0} = 0, \quad C_z^-|_{z=l_z} = 0, \quad C_x^+|_{x=0} = 0, \quad C_x^-|_{x=l_x} = 0. \tag{19}$$

To solve the boundary problem defined by Eqs. (12) and (19), we introduce functions $F_z = (C_z^+ + C_z^-)$ and $F_x = (C_x^+ + C_x^-)$ and rewrite Eqn. (12) in the form

$$\begin{aligned} \frac{\partial^2 F_z}{\partial z^2} + \delta^2 F_z &= -2\alpha\delta F_x, \\ \frac{\partial^2 F_x}{\partial x^2} + \delta^2 F_x &= -2\alpha\delta F_z, \end{aligned} \tag{20}$$

with boundary conditions (19) taking the following form:

$$\begin{aligned} \left(\frac{\partial F_z}{\partial z} \mp i\delta F_z\right)\Big|_{z=l_z/2\pm l_z/2} &= 0, \\ \left(\frac{\partial F_x}{\partial x} \mp i\delta F_x\right)\Big|_{x=l_x/2\pm l_x/2} &= 0. \end{aligned} \tag{21}$$

First, we find eigenfunctions $f_\xi(\xi)$ of the operator

$$T_\xi = \frac{d^2}{d\xi^2}, \tag{22}$$

with boundary conditions $.(\frac{\partial f_\xi}{\partial \xi} \mp i\delta f_\xi)|_{z=l_\xi/2\pm l_\xi/2} = 0$ corresponding to an eigenvalue Λ_ξ^2, $T_\xi f_\xi(\xi) = \Lambda_\xi^2 f_\xi(\xi)$, in the form

$$\begin{aligned} f_\xi(\xi) = (\delta + \Lambda_\xi)\exp[i\Lambda_\xi(\xi + l_\xi/2)] \\ - (\delta - \Lambda_\xi)\exp[-i\Lambda_\xi(\xi - l_\xi/2)]. \end{aligned} \tag{23}$$

The eigenvalue satisfies the characteristic equation:

$$\exp(2i\Lambda_\xi l_\xi) = \frac{(\delta - \Lambda_\xi)^2}{(\delta + \Lambda_\xi)^2}. \tag{24}$$

Then, using expression (23), we find the solutions of Eq. (20) after the variables separation, i.e., seeking $F_{x,z}$ as

$$F_z(x,z) \sim F_x(x,z) \sim f_x(x)\, f_z(z). \tag{25}$$

Substituting (25) into (20), we obtain from the condition of a nontrivial solution [compare to (18)]:

$$\left(\delta^2 - \Lambda_x^2\right)\left(\delta^2 - \Lambda_z^2\right) = 4\alpha^2\delta^2. \tag{26}$$

Eigenvalues Λ_x^2 and Λ_z^2 of the T_x and T_z operators, correspondingly, can be found from the characteristic equations:

$$\begin{aligned} \exp(2i\Lambda_z l_z) &= \frac{(\delta - \Lambda_z)^2}{(\delta + \Lambda_z)^2}, \\ \exp(2i\Lambda_x l_x) &= \frac{(\delta - \Lambda_x)^2}{(\delta + \Lambda_x)^2}. \end{aligned} \tag{27}$$

Joint solution $\delta(\alpha,l_x,l_z)$, $\Lambda_x(\alpha,l_x,l_z)$, $\Lambda_z(\alpha,l_x,l_z)$ of the algebraic equations (26) and (27) determines the discrete spectrum of complex resonator eigenfrequencies δ and the structure of eigenmodes.

To find the spatial structures of partial waves for a given eigenmode, we substitute (25) and (23) into (12). Integrating it with boundary conditions (19), we obtain

$$\begin{aligned} C_z^\pm &= 2i\alpha(\delta \pm \Lambda_z)\exp(\pm i\Lambda_z l_z/2)\sin[\Lambda_z(z \pm l_z/2)]f_x(x), \\ C_x^\pm &= 2i\alpha(\delta \pm \Lambda_x)\exp(\pm i\Lambda_x l_x/2)\sin[\Lambda_x(x \pm l_x/2)]f_z(z). \end{aligned} \tag{28}$$

Under conditions of strong coupling of waves $\alpha l_{x,z} \gg 1$, solutions of (26) and (27) which determine the eigenvalues (eigenfrequencies) of the boundary problem (12) and (19) can be given in the explicit form [9]:

$$\delta_{n,m} = \pm\frac{\pi^2 mn}{2\alpha\, l_z l_x} + i\frac{\pi^2}{2\alpha^2\, l_z l_x}\left(\frac{n^2}{l_z} + \frac{m^2}{l_x}\right), \tag{29a}$$

$$\delta_{n,m} = \pm\left[2\alpha + \frac{\pi^2}{4\alpha}\left(\frac{n^2}{l_z^2} + \frac{m^2}{l_x^2}\right)\right] + i\frac{\pi^2}{2\alpha^2}\left(\frac{n^2}{l_z^3} + \frac{m^2}{l_x^3}\right), \tag{29b}$$

where $n = 0,1,2\ldots$ and $m = 0,1,2\ldots$ are the subscripts of modes along the longitudinal and transverse coordinates.

Frequencies and Q factors of eigenmodes are determined, respectively, by the real and imaginary parts of the eigenvalue $\delta_{n,m}$:

$$\omega_{n,m} = c\bar{h} + c\mathrm{Re}\delta_{n,m}, \tag{30a}$$

$$Q_{n,m} = \bar{h}/2\mathrm{Im}\delta_{n,m}. \tag{30b}$$

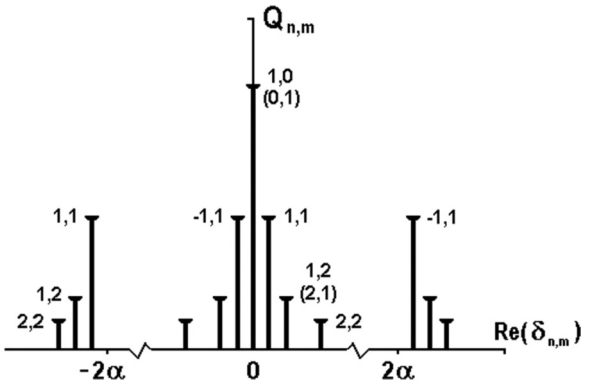

FIG. 3. Eigenmode spectrum of 2D Bragg resonators.

According to (29), 2D Bragg resonators possess high selectivity with respect to both the longitudinal (n) and the transverse (m) mode subscripts. Resonator eigenmodes (Fig. 3) are located in the vicinity of the precise Bragg frequency,

$$\omega \approx c\bar{h}, \tag{31a}$$

as well as in the vicinity of edges of the Bragg reflection zone (Bragg stop zone),

$$\omega \approx c\bar{h} \pm 2\alpha. \tag{31b}$$

Eigenmodes given by (31b) are similar to those of 1D Bragg resonators and are associated with the sheet 1 of the normal waves' dispersion characteristics (in Fig. 2). A specific feature of 2D Bragg resonators is the existence of high-Q eigenmodes (31a) in the middle of the Bragg reflection zone without any corrugation defects. Those eigenmodes are associated with the sheet "2" of the normal waves dispersion characteristics. Maximum-Q eigenmodes are those with subscripts $\{n = 0,\ m = 1\}$ and $\{n = 1,\ m = 0\}$ (Fig. 3). These eigenmodes are degenerate with respect to the frequency which coincides with the Bragg frequency in the considered geometric optics approximation. In the case of $l_x = l_z$, those modes are also degenerate with respect to the Q factor. To remove this degeneracy, a rectangular-shaped structure can be used instead of a square-shaped one. The mode with the subscripts $\{n = 1,\ m = 0\}$ has the highest Q factor at $l_z > l_x$,

$$Q_{1,0} = \frac{\bar{h}k^2\alpha^2 {l_z}^2 l_x}{\pi^2}. \tag{32}$$

Field structures of partial waves of the fundamental eigenmode for $l_z = 2l_x$ are presented in Fig. 4.

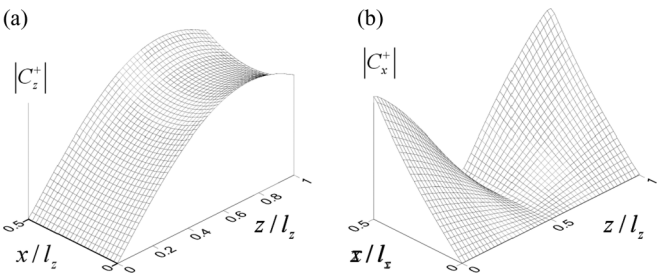

FIG. 4. Spatial distributions of the partial waves forming the fundamental eigenmode at $\alpha l_z = 2$, $l_z = 2l_x$.

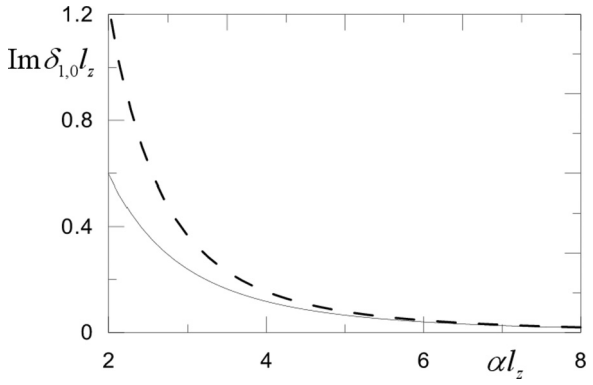

FIG. 5. Dependence of fundamental mode decrement on the resonator dimensions at $l_z = 2l_x$; dashed line shows analytical dependence in the approximation of $\alpha l_z \gg 1$.

To define more exactly the value of the fundamental mode Q factor at relatively small values of $\alpha l_{x,z}$ we solved Eqs. (26) and (27) numerically using the particle swarm optimization (PSO) method [30]. Results presented in Fig. 5 demonstrate that relation (28) yields good approximation for the Q factor at $\alpha l_z > 2$, $l_z = 2l_x$.

Relations (2), (6)–(8), (13), (23), (28), and (29) give a fully analytical description of the highest quality TM-TM eigenmodes of dielectric films with corrugation that are oversized in lateral dimensions (1); relations (2), (9)–(11), (16), (23), (28) and (29) describe TE-TM eigenmodes in those structures.

It is important to emphasize that within the framework of assumptions being used (geometrical optics), ratios of the Q-factors of different eigenmodes are independent of the dimensions l_z, l_x of the Bragg structure. It means that the system sustains its selectivity at increasing those dimensions if we ignore such factors as Ohmic losses. One should also note that the existence of modes in the middle of the Bragg resonance band in the absence of periodicity defects is a specific feature of the 2D Bragg structures, which distinguishes them both from 1D (single-periodic) prototypes [15–17] and 2D photonic crystals [31,32], where periodicity defects are typically required to produce modes.

III. NONLINEAR DYNAMICS

Next, we consider a thin layer of active medium located in the middle of the waveguide ($y = 0$) with the thickness being small in the scale of inhomogeneity of the lowest waveguide mode. The spatiotemporal dynamics of 2D DFL will be described in the framework of the semiclassical approach based on Maxwell-Bloch equations [33].

$$\left[\Delta - \frac{\varepsilon(x,z)}{c^2}\frac{\partial^2}{\partial t^2}\right] A = -\frac{4\pi}{c} P,$$
$$\frac{\partial^2 P}{\partial t^2} + \frac{1}{T_2}\frac{\partial P}{\partial t} + \left(\frac{1}{4{T_2}^2} + {\omega_0}^2\right) P = -\frac{2\omega_0 |\mu|^2}{\hbar c} A\rho, \tag{33}$$
$$\frac{\partial \rho}{\partial t} + \frac{\rho - \rho_e}{T_1} - D\Delta\rho = \frac{2}{\hbar\omega_0 c} A\frac{\partial P}{\partial t}.$$

Here ρ_e is an equilibrium value of population inversion, μ is the dipole moment, T_1 and T_2 are the relaxation time constants,

ω_0 is the transition frequency, and D is the diffusion coefficient of the nonequilibrium carriers.

In time domain, coupled-wave equation (12), taking into account partial waves amplification by an active medium, acquires the form

$$\left(\pm\frac{\partial}{\partial Z}+\frac{\partial}{\partial\tau}\right)\hat{C}_z^{\pm}+i\hat{\alpha}(\hat{C}_x^{+}+\hat{C}_x^{-})=\hat{P}_z^{\pm},$$
$$\left(\pm\frac{\partial}{\partial X}+\frac{\partial}{\partial\tau}\right)\hat{C}_x^{\pm}+i\hat{\alpha}(\hat{C}_z^{+}+\hat{C}_z^{-})=q\hat{P}_x^{\pm}. \tag{34}$$

In Eq. (34), we introduced the following normalized variables and parameters: $\hat{X}=xr^{-1}/l_z$, $\hat{Z}=zr/l_z$, $\hat{\tau}=v_g t/l_z$, $\hat{C}_x^{\pm}=C_x^{\pm}(\frac{b^{\rm eff}\omega_0}{\pi\rho_e\hbar c v_g b_\rho r})^{1/2}$, $\hat{C}_z^{\pm}=C_z^{\pm}(\frac{b^{\rm eff}\omega_0 r}{\pi\rho_e\hbar c v_g b_\rho})^{1/2}$; $\hat{P}_z^{\pm}=P_z^{\pm}(\frac{\pi b_\rho l_z}{\rho_e\hbar\omega_0 c v_g b^{\rm TE} r})^{1/2}$, $P_z^{\pm}$ are the corresponding components of polarization induced in the active medium.

Next, we consider two cases:

(a) all four partial TM waves are amplified equally by the active medium: $q=1$, $b^{\rm eff}=b^{\rm TM}$;

(b) only TE-polarized waves $\hat{C}_z^{\pm}$ are amplified: $q=0$, $b^{\rm eff}=b^{\rm TE}$.

The first case corresponds to the coupling of four TM modes being amplified by a semiconductor active medium while the second case describes coupling of TE and TM modes in a quantum-well laser with only TE modes being amplified.

Taking into account the field presentation (2) as a sum of four partial waves we put down the polarization and population inversion in the following form [33]:

$$\begin{aligned}P=&\,\mathrm{Re}\big[i\big(P_z^{+}e^{i\bar{h}z}+P_z^{-}e^{-i\bar{h}z}\\&+qP_x^{+}e^{i\bar{h}x}+qP_x^{-}e^{-i\bar{h}x}\big)e^{i\omega_0 t}\big],\\ \rho=&\,\rho_0+\mathrm{Re}\big(\rho_{2z}e^{2i\bar{h}z}+q\rho_{2x}e^{2i\bar{h}x}+q\rho_{z-x}e^{2i\bar{h}(z-x)}\\&+q\rho_{z+x}e^{2i\bar{h}(z+x)}\big).\end{aligned} \tag{35}$$

Here $P_{x,z}^{\pm}$, ρ_0, ρ_{2z}, ρ_{2x}, ρ_{z-x}, ρ_{z+x} are the slowly varying amplitudes, ρ_0 is the average population inversion, and ρ_{2z}, ρ_{2x}, ρ_{z-x}, ρ_{z+x} correspond to the inversion gratings induced by the standing electromagnetic waves due to the effect of spatial hole burning. Components of population inversion satisfy the following equations:

$$\begin{aligned}\frac{\partial\hat{\rho}_0}{\partial\tau}+\frac{(\hat{\rho}_0-1)}{\hat{T}_1}=&-(\hat{C}_z^{+}\hat{P}_z^{+*}+\hat{C}_z^{-}\hat{P}_z^{-*}+q\hat{C}_x^{+}\hat{P}_x^{+*}\\&+q\hat{C}_x^{-}\hat{P}_x^{-*}),\\ \frac{\partial\hat{\rho}_{2z}}{\partial\tau}+\frac{\hat{\rho}_{2z}}{\hat{T}_D}=&-(\hat{C}_z^{+}\hat{P}_z^{-*}+\hat{C}_z^{-}\hat{P}_z^{+*}),\\ \frac{\partial\hat{\rho}_{2x}}{\partial\tau}+\frac{\hat{\rho}_{2x}}{\hat{T}_D}=&-q(\hat{C}_x^{+}\hat{P}_x^{-*}+\hat{C}_x^{-}\hat{P}_x^{+*}),\\ \frac{\partial\hat{\rho}_{z+x}}{\partial\tau}+\frac{\hat{\rho}_{z+x}}{\hat{T}_D}=&-q(\hat{C}_z^{+}\hat{P}_x^{-*}\\&+\hat{C}_z^{-*}\hat{P}_x^{+}+\hat{C}_x^{+}\hat{P}_z^{-*}+\hat{C}_x^{-*}\hat{P}_z^{+}),\\ \frac{\partial\hat{\rho}_{z-x}}{\partial\tau}+\frac{\hat{\rho}_{z-x}}{\hat{T}_D}=&-q(\hat{C}_z^{+}\hat{P}_x^{+*}+\hat{C}_z^{-*}\hat{P}_x^{-}\\&+\hat{C}_x^{+*}\hat{P}_z^{+}+\hat{C}_x^{-}\hat{P}_z^{-*}),.\end{aligned} \tag{36}$$

where $\hat{T}_1=\frac{v_g T_1}{l_z}$, $\hat{T}_D=\frac{v_g}{l_z(T_1^{-1}+Dh^2)}$, $\hat{\rho}=\frac{\rho}{\rho_e}$.

Assuming that the transverse relaxation time T_2 is small comparing to other time values we apply the balance approximation [33] which gives the following expressions for the components of polarization:

$$\begin{aligned}\hat{P}_z^{+}&=\beta(2\hat{C}_z^{+}\hat{\rho}_0+\hat{C}_z^{-}\hat{\rho}_{2z}+q\hat{C}_x^{+}\hat{\rho}_{z-x}+q\hat{C}_x^{-}\hat{\rho}_{z+x}),\\ \hat{P}_z^{-}&=\beta(2\hat{C}_z^{-}\hat{\rho}_0+\hat{C}_z^{+}\hat{\rho}_{2z}^{*}+q\hat{C}_x^{+}\hat{\rho}_{z+x}^{*}+q\hat{C}_x^{-}\hat{\rho}_{z-x}^{*}),\\ \hat{P}_x^{+}&=q\beta(2\hat{C}_x^{+}\hat{\rho}_0+\hat{C}_x^{-}\hat{\rho}_{2x}+\hat{C}_z^{+}\hat{\rho}_{z-x}^{*}+\hat{C}_z^{-}\hat{\rho}_{z+x}),\\ \hat{P}_x^{-}&=q\beta(2\hat{C}_x^{-}\hat{\rho}_0+\hat{C}_x^{+}\hat{\rho}_{2z}^{*}+\hat{C}_z^{+}\hat{\rho}_{z+x}^{*}+\hat{C}_z^{-}\hat{\rho}_{z-x}),\end{aligned} \tag{37}$$

where $\beta=\pi\rho_e|\mu|^2 b_\rho l_z T_2 c/2\hbar\omega_0 b^{\rm eff}$ describes normalized pump intensity and in fact defines the linear gain of active medium [see Eq.(44)]. Boundary conditions for Eqs. (33) and (36) coincide with (19):

$$\hat{C}_z^{-}|_{Z=1}=0,\ \hat{C}_z^{+}|_{Z=0}=0,\ \hat{C}_x^{-}|_{X=L_x}=0,\ \hat{C}_x^{+}|_{X=0}=0, \tag{38}$$

where $L_x=l_x/l_z$.

The total output power can be defined in the following way:

$$S=\frac{\rho_e\hbar\omega_0 b_\rho v_{gr} l_z}{4}\hat{S}, \tag{39}$$

where

$$\begin{aligned}\hat{S}=&\,r^{-1}\int_0^{L_x}(|\hat{C}_z^{+}(X,L_z)|^2+|\hat{C}_z^{-}(X,0)|^2)dX\\&+r\int_0^{1}(|\hat{C}_x^{+}(L_x,Z)|^2+|\hat{C}_x^{-}(0,Z)|^2)dZ.\end{aligned}$$

In normalized variables, the energy balance relation in the steady-state lasing regime can be presented as follows:

$$\hat{S}+\frac{\langle\hat{\rho}_0\rangle L_x}{\hat{T}_1}=\frac{L_x}{\hat{T}_1}, \tag{40}$$

where $\langle\rho_0\rangle=\int_0^1\int_0^{L_x}\hat{\rho}_0 dX dZ/L_x$ is the average population inversion which determines laser efficiency:

$$\eta=\frac{1-\langle\hat{\rho}_0\rangle}{\hat{T}_1}. \tag{41}$$

Note that Eq. (40) expresses balance between laser radiation power and spontaneous relaxation and includes no other kind of losses.

We studied the nonlinear dynamics by solving numerically Eqs. (34) and (36) with boundary conditions (38). For initial conditions, we took noise distribution of the electromagnetic field with a small amplitude $c_0\ll 1$:

$$\hat{C}_{x,z}^{\pm}(X,Z,\tau=0)=c_0 e^{-i\varphi_{x,z}^{\pm}(X,Z)}, \tag{42}$$

where $\varphi_x^{+}(X,Z)$, $\varphi_x^{-}(X,Z)$,$\varphi_z^{+}(X,Z)$, $\varphi_z^{-}(X,Z)$ are evenly distributed functions completely random at every simulation point.

A. Simulation results for the case of TM-TM wave coupling

In this case, all four partial waves are amplified indiscriminately ($q=1$) regardless of directions of their propagation. To describe the self-excitation condition, we linearize Eqs. (34)

and (36) as

$$\pm\frac{\partial\hat{C}_z^{\pm}}{\partial Z}+\frac{\partial\hat{C}_z^{\pm}}{\partial\tau}-2\beta\hat{C}_z^{\pm}=i\hat{\alpha}(\hat{C}_x^{+}+\hat{C}_x^{-}),$$
$$\pm\frac{\partial\hat{C}_x^{\pm}}{\partial X}+\frac{\partial\hat{C}_x^{\pm}}{\partial\tau}-2\beta\hat{C}_x^{\pm}=i\hat{\alpha}(\hat{C}_z^{+}+\hat{C}_z^{-}). \quad (43)$$

In the case of $\hat{\alpha}\gg 1$, the self-excitation conditions for the different modes can be written in the form

$$\mathrm{Im}\frac{c\delta_{n,m}}{\alpha\omega_0}=2\beta, \quad (44)$$

where the mode decrements are determined by relations (29). The self-excitation threshold is realized for the fundamental mode and can be presented in the form

$$4\beta\hat{\alpha}^2L_x/\pi^2=1. \quad (45)$$

Imprecision of the strong coupling approximation solution (29) when compared to direct numerical solution of Eqs. (25) and (26) at lower coupling values is demonstrated in Fig. 5, which shows that the analytical solution (45) correctly estimates the self-excitation threshold at $\hat{\alpha}>3$.

For simulation of the laser excitation process we take $\hat{\alpha}=2$, at which the most uniform field distribution across the resonator is achieved. We neglect the effect of nonequilibrium carrier diffusion assuming $D=0$ for now, which is correct for many types of laser media where the laser transition takes place between loosely coupled atom energy levels.

In the case of a moderate threshold excess, a stationary lasing regime takes place (Fig. 6). Increasing the pump intensity leads to laser power and efficiency increase until at a certain gain level the steady-state regime is replaced by a self-modulation lasing regime. Figure 7 presents amplitude profiles of the partial waves at different moments of time inside the 2D active medium demonstrating the stages of the steady-state lasing regime establishment. During the first stage $\tau<1$, the field distributions are completely random with the scale of inhomogeneity corresponding to the initial random conditions (42). After a few passes of partial waves across the resonator $\tau<3$, the inhomogeneity scale of the amplitude profile becomes comparable to the geometric dimensions of the structure. Taking into account similar behavior of instant phase distribution, it can be interpreted as spatial synchronization.

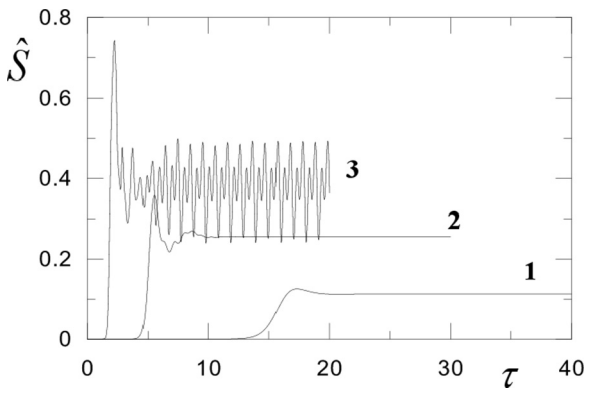

FIG. 6. Time dependencies of the normalized output power. Establishment of the steady-state and self-modulation regimes at (1) $\beta=1$, (2) $\beta=2$, (3) $\beta=6$; $\hat{\alpha}=2$, $\hat{T}_1=\hat{T}_D=1$.

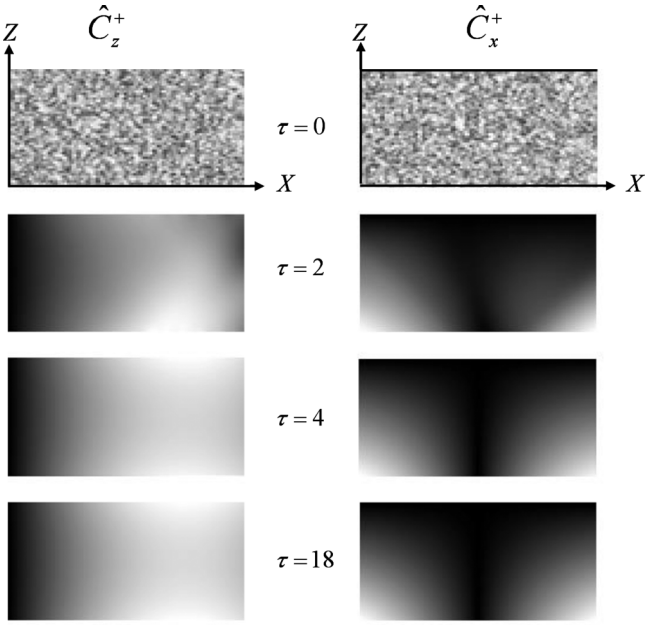

FIG. 7. Evolution of partial wave spatial distributions during the establishment of the steady-state lasing regime; $\hat{\alpha}=2$, $\beta=1$, $\hat{T}_1=\hat{T}_D=1$.

The next stage (up to $\tau\approx 4$) is the stage of selection of the fundamental mode when amplitude profiles get closer to the profile of fundamental modes shown in Fig. 4. Note that at that moment the amplitudes of partial waves are low (far from saturation) and interaction is still linear. Then the amplitudes grow and the interaction reaches the nonlinear stage, at which the field profiles transform from the fundamental mode profiles to the stationary lasing regime distributions ($\tau>18$). In the simulated case of a relatively small threshold excess $\beta=1$, steady-state field distributions are closer to those of the fundamental mode (Fig. 4). However, at larger threshold excess values ($\beta=2$), a significant distortion of the field distributions occurs (Fig. 8). This is caused by development of spatial inhomogeneity of population inversion. Spectrum analysis shows that the generation frequency in the steady-state lasing regime is close to the Bragg frequency.

A certain scaling law follows from stationary solutions of Eqs. (34) and (36). If we decrease the normalized relaxation time of the population inversion $\hat{T}_1$, the amplitude profiles of the partial waves in the steady-state lasing regime do not change. At the same time, the wave amplitudes and the normalized output power increase proportionally (Fig. 9):

$$\left|\hat{C}_{x,z}^{\pm}\right|\sqrt{\hat{T}_1}=\mathrm{const},\quad \left|\hat{P}_{x,z}^{\pm}\right|\sqrt{\hat{T}_1}=\mathrm{const},\quad \hat{S}\hat{T}_1=\mathrm{const}. \quad (46)$$

In physical variables, it means that if the sizes $l_{x,z}$ of the active region are increased while the equilibrium population inversion ρ_e (for example, by decreasing the pump power density) and the coupling coefficient α are proportionally decreased so that

$$l_{x,z}\rho_e=\mathrm{const}\ \text{ and }\ l_{x,z}\alpha=\mathrm{const}, \quad (47)$$

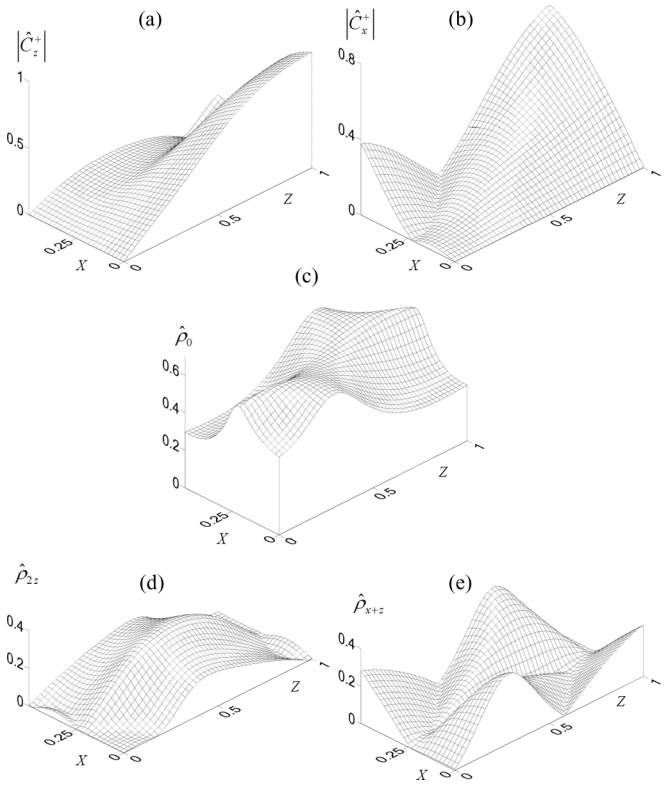

FIG. 8. Spatial distributions of the partial waves and population inversion components in the steady-state regime at $\hat{\alpha} = 2$, $\beta = 2$, $\hat{T}_1 = \hat{T}_D = 1$.

the amplitude distribution of the partial waves in the stationary lasing regime will not change but the total output power will increase proportionally:

$$S/l_{x,z} = \text{const}. \tag{48}$$

Simulations of the lasing dynamics with the help of Eqs. (34) and (36) show that the stationary regime establishes in the entire range of $\hat{T}_1$ values admissible from the point of view of computational resources. Meanwhile transient processes change with varying $\hat{T}_1$ because they depend on the ratio between the relaxation time $\hat{T}_1$ and the lifetime of photons in the resonator $T_p = 1/\text{Im}\delta_{10}$. At $\hat{T}_1 \gg T_p$, on the initial stage

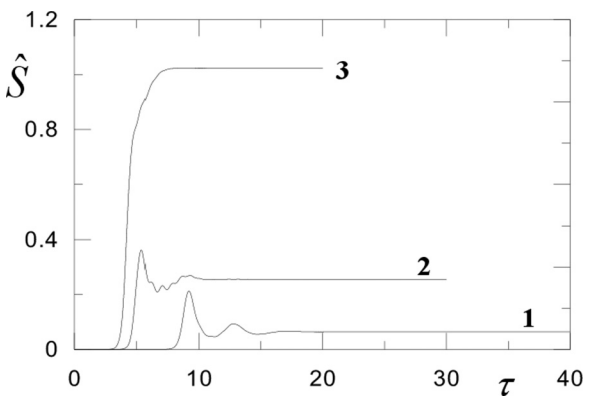

FIG. 9. Time dependencies of normalized output power at (1) $\hat{T}_1 = 4$, (2) $\hat{T}_1 = 1$, (3) $\hat{T}_1 = 0.25$; $\hat{\alpha} = 2$, $\beta = 2$, $\hat{T}_D = 1$.

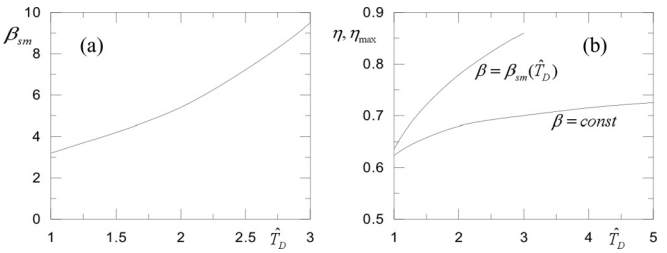

FIG. 10. Dependences of the self-modulation threshold β_{sm} (a) and laser efficiency (b) from the diffusion time $\hat{T}_D$; $\hat{\alpha} = 2$, $\hat{T}_1 = 1$. Dashed and solid lines in (b) show dependencies at constant $\beta = 3$ and at $\beta = \beta_{sm}(\hat{T}_D)$ pump intensities, respectively.

of transient process, a pulse with the peak power significantly exceeding the output power in the stationary lasing regime is generated (Fig. 9).

Note that if we increase the threshold excess β significantly, i.e., increase pump intensity or the Bragg resonator quality, periodic and then stochastic self-modulation regimes will take place (curve 3 in Fig. 6).

Note that all of the above analysis was made under assumption of no significant diffusion of population inversion. However, nonequilibrium carriers in semiconductor laser media usually travel freely along quantum wells. This results in significant diffusion which counters the effect of spatial hole burning by reducing or, in the case of $D\bar{h}_z^2 \gg \hat{T}_1^{-1}$, by completely removing dynamic gratings $\rho_{2z,2x}$ and $\rho_{z\pm x}$ [see Eq. (36)]. This increases the self-modulation threshold β_{sm} at which the single-mode steady-state regime transforms into a multimode regime [Fig. 10(a)]. As a result, countering spatial hole burning improves laser efficiency in two ways as shown in Fig. 10(b): firstly, by increasing radiation power at a constant pump level $\beta = \text{const}$ and secondly, by allowing higher pump intensity $\beta < \beta_{sm}(\hat{T}_D)$ with greater efficiency while maintaining the steady-state lasing regime.

B. Simulation results for the case of TM-TE wave coupling

In the case when only TE-polarized partial waves ($\hat{C}_z^{\pm}$) are amplified in the active medium ($q = 0$), the laser's dynamics are quite similar to the case described above. On the linear

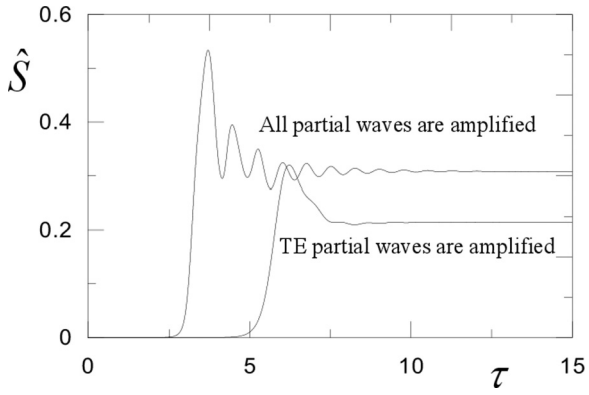

FIG. 11. Time dependencies of the normalized output power in cases where all four or only TE-polarized ($C_z^{\pm}$) partial waves are amplified; $\beta = 3$; $\hat{\alpha} = 2$, $\hat{T}_1 = \hat{T}_D = 1$.

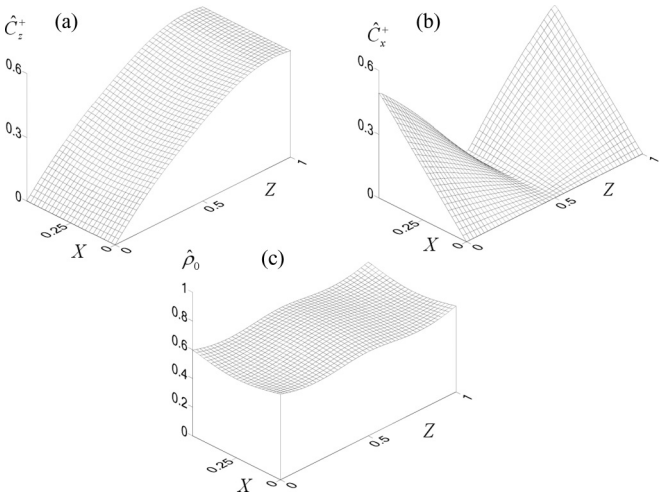

FIG. 12. Spatial distributions of the partial waves and the average population inversion in the steady-state regime in cases where only TE-polarized ($C_z^{\pm}$) partial waves are amplified; $\beta = 2$; $\hat{\alpha} = 2$, $\hat{T}_1 = \hat{T}_D = 1$.

stages the most noticeable differences are the increased self-excitation threshold and the decreased increment. This can result in a much longer linear stage and less power output in the stationary lasing regime when operating too close to the threshold (Fig. 11). Partial wave field distributions in the stationary lasing regime are presented in Fig. 12, and in this case they are similar to the field distributions in the fundamental mode of a 2D Bragg resonator. However, in the case of TM-TM wave coupling, steady-state distributions are quite different (see Fig. 8). Components ρ_{z-x} and ρ_{z+x} of the inversion produce additional coupling between the partial waves on the nonlinear stage of the interaction and change the stationary regime amplitude distributions. With only two of the partial waves amplified, both population inversion and electromagnetic field distributions get simplified. The self-modulation regime threshold is also increased which allows achieving higher power output and efficiency in the stationary lasing regime by using higher pump intensity.

Simulation results allow us to estimate the output power and some other parameters of 1 μm 2D DFB lasers. According to the analysis given above, for an active region with a length of $l_z = 2$ mm and a width of $l_x = 0.5$ mm, respectively, and for a linear gain value of 15 cm^{-1} (typical for InGaP-GaAs heterolasers), the output power would achieve about $S = 1$ W in the steady-state regime. Transverse structure of heterolasers should include about $b_0 = 600$-nm-thick GaAs waveguide layer with about $2b_1 = 35$-nm-deep corrugation of its surface to produce enough coupling for the partial TE and TM waves.

IV. CONCLUSION

In this paper, we use a coupled-wave method to describe eigenmodes of 2D Bragg resonators formed by double-periodically corrugated dielectric layer. The analysis considers eigenmodes composed of both TM and TE waveguide modes. In fact, we have obtained the analytical expressions for the highest-quality modes of corrugated dielectric films, oversized in lateral dimensions. We have shown that 2D Bragg resonators possess high selectivity over both the longitudinal and the transverse indices with the fundamental mode being in the middle of the stop band. Note that a 2D Bragg resonator in terms of photonic band-gap structures corresponds to a photonic crystal without side reflections operating near the "M" symmetry point in the reciprocal space [28]. Thus according to our analysis, a structure with periodicity given by (1) or (4) provides the existence of high-Q eigenmodes near the M point without any periodicity defects.

Nonlinear dynamics of 2D distributed feedback lasers based on 2D Bragg resonators was studied using a semiclassical approach in the case of all partial waves amplified equally as well as in the case of quantum-well lasers where only TE waveguide modes are amplified. Scalability features of 2D distributed feedback lasers are discussed to demonstrate possibility of dramatic increasing of output power by increasing size of active medium while still maintaining the synchronization regime.

Note also that in this paper we study only static 2D Bragg grating based on modulation of the effective refraction index. However, there is an alternative way of producing distributed feedback, namely, a periodic gain modulation. Apparently, this method is also applicable to 2D DFB lasers. Dynamic 2D gain grating can be achieved by illuminating the active layer with two couples of pumping wave beams with orthogonal wave vectors directed as the grating vectors in Fig. 1.

ACKNOWLEDGMENTS

This work was supported in part by the Russian Foundation for Basic Researches under Grants No. 14-02-31493 and No. 13-02-97130.

[1] N. S. Ginzburg, N. Yu. Peskov, and A. S. Sergeev, Pis'ma v ZhTF, **18**(9), 23 (1992) (in Russian).
[2] N. S. Ginzburg, N. Yu. Peskov, and A. S. Sergeev, Opt. Commun. **112**, 151 (1994).
[3] N. S. Ginzburg, N. Yu. Peskov, A. S. Sergeev, A. D. R. Phelps, I. V. Konoplev, G. R. M. Robb, A. W. Cross, A. V. Arzhannikov, and S. L. Sinitsky, Phys. Rev. E **60**, 935 (1999).
[4] M. Toda, IEEE J. Quantum Electron. **28**, 1653 (1992).
[5] M. Yokoyama and S. Noda, Opt. Express **13**, 2869 (2005).
[6] C. Peng, Y. Liang, K. Sakai, S. Iwahashi, and S. Noda, Opt. Express **19**, 24672 (2011).
[7] H. Han and J. J. Coleman, IEEE J. Quantum Electron. **31**, 1947 (1995).
[8] V. R. Baryshev, N. S. Ginzburg, A. M. Malkin, and A. S. Sergeev, Acta Phys. Pol. A **112**, 897 (2007).
[9] V. R. Baryshev, N. S. Ginzburg, and A. S. Sergeev, Tech. Phys. Lett. **34**, 113 (2008).
[10] N. S.Ginzburg, V. R. Baryshev, A. M. Malkin, and A. S. Sergeev, Opt. Commun. **281**, 4979 (2008).
[11] N. S. Ginzburg, N. Yu. Peskov, A. S. Sergeev, V. Yu. Zaslavsky, A. W. Cross, W. He, I. V. Konoplev, A. D. R. Phelps, C. W. Robertson, K. Ronald, C. G. Whyte, A. V. Arzhannikov, P. V.

Kalinin, S. A. Kuznetsov, S. L. Sinitsky, V. D. Stepanov, and M. Thumm, IEEE Trans. Plasma Sci. **37**, 1792 (2009).
[12] I. V. Konoplev, A. W. Cross, A. D. R. Phelps, W. He, K. Ronald, C. G. Whyte, C. W. Robertson, P. MacInnes, N. S. Ginzburg, N. Y. Peskov, A. S. Sergeev, V. Y. Zaslavsky, and M. Thumm, Phys. Rev. E **76**, 056406 (2007).
[13] N. S. Ginzburg, N. Yu. Peskov, A. S. Sergeev, G. G. Denisov, S. V. Kuzikov, V. Yu. Zaslavsky, A. V. Arzhannikov, P. V. Kalinin, S. L. Sinitsky, and M. Thumm, Appl. Phys. Lett. **92**, 103512 (2008).
[14] A. V. Arzhannikov, N. S. Ginzburg, V. Yu. Zaslavsky, V. G. Ivanenko, I. A. Ivanov, P. V. Kalinin, A. S. Kuznetsov, S. A. Kuznetsov, N. Yu. Peskov, A. S. Sergeev, S. L. Sinitsky, and V. D. Stepanov, JETP Lett. **87**, 618 (2008).
[15] A. Yariv, *Quantum Electronics* (Wiley, New York, 1975).
[16] H. Kogelnik and C. V. Shank, J. Appl. Phys. **43**, 2327 (1972).
[17] H. Ghafouri-Shiraz, *Distributed Feedback Laser Diodes and Optical Tunable Filters* (Wiley, New York, 2003).
[18] A. P. Bogatov, A. E. Drakin, A. A. Stratonnikov, and V. P. Konyaev, Quantum Electron. **30**, 401 (2000).
[19] D. V. Batrak and A. P. Bogatov, Quantum Electron. **37**, 745 (2007).
[20] G. S. Sokolovskii, V. V. Dudelev, I. M. Gadzhiev, S. N. Losev, A. G. Deryagin, V. I. Kuchinskii, E. U. Rafailov, and W. Sibbett, Tech. Phys. Lett. **31**, 824 (2005).
[21] A. Sarangan, M. Wright, J. Marciante, and D. Bossert, IEEE J. Quantum Electron. **35**, 1220 (1999).
[22] X. K. Sun and A. Yariv, Opt. Express **16**, 9155 (2008).
[23] N. Yu. Gordeev, I. I. Novikov, A. M. Kuznetsov, Yu. M. Shernyakov, M. V. Maximov, A. E. Zhukov, A. V. Chunareva, A. S. Payusov, D. A. Livshits, and A. R. Kovsh, Semiconductors **44**, 1357 (2010).
[24] T. Erdogan and D. G. Hall, J. Appl. Phys. **68**, 1435 (1990).
[25] C. Wu, T. Makino, S. I. Najafi, R. Maciejko, M. Svilans, J. Glinski, and M. Fallahi, IEEE J. Quantum Electron. **29**, 2596 (1993).
[26] M. Asada, A. Kameyama, and Y. Suematsu, IEEE J. Quantum Electron. **20**, 745 (1984).
[27] C. Aversa and K. Iizuka, IEEE J. Quantum Electron. **28**, 1864 (1992).
[28] C. C. Davis, *Lasers and Electro-Optics: Fundamentals and Engineering* (Cambridge University Press, New York, 2014).
[29] H. Kogelnik, Theory of dielectric waveguides, in *Integrated Optics*, Topics in Applied Physics Vol. 7 (Springer, Berlin/Heidelberg, 1979), pp. 13–81.
[30] J. Kennedy and R. C. Eberhart, *Swarm Intelligence*, The Morgan Kaufmann Series in Evolutionary Computation (Academic Press, New York, 2001).
[31] E. Yablonovitch, Phys. Rev. Lett. **58**, 2059 (1987).
[32] S. John, Phys. Rev. Lett. **58**, 2486 (1987).
[33] A. V. Andreev, Sov. Phys. Usp. **33**, 997 (1990).